Vibratory power flow through a nonlinear path into a resonant receiver

T. J. Royston[a)]
Vibrations and Acoustics Laboratory, Department of Mechanical Engineering, The University of Illinois at Chicago, Chicago, Illinois 60607-7022

R. Singh
Acoustics and Dynamics Laboratory, Department of Mechanical Engineering, The Ohio State University, Columbus, Ohio 43210-1107

(Received 20 June 1996; accepted for publication 2 December 1996)

Vibratory power flow through a nonlinear path into a resonant receiver is considered via a specific vibration isolation example case, the automotive hydraulic engine mount. System equations for the source—nonlinear path—receiver system are developed based on prior experimental and analytical studies. For periodic excitation, an efficient solution method is formulated for the calculation of the steady-state stable response using a multi-term harmonic balance approach with condensation and continuation. In this computational study it is shown that, while modeling the isolation path with a ''softened'' nonlinear expression may only moderately alter the predicted system behavior at the excitation harmonic, it can significantly alter it at higher harmonics. Computational studies of multi-harmonic motion and power transmission show that audible structure-borne noise may be generated from subaudio frequency excitations due to path nonlinearities. It is also observed that support base (receiver) resonances can significantly affect the overall dynamic behavior. For instance, with a multi-degree-of-freedom base model, significant levels of vibratory energy at higher harmonics of the excitation are transmitted through the path, especially when these harmonics coincide with the natural frequencies of the receiver. [S0001-4966(97)04504-9]

PACS numbers: 43.40.At, 43.25.Ts, 43.40.Tm [CBB]

INTRODUCTION

Fundamental studies of vibration isolation in *linear* systems have shown that compliant support structure dynamics can significantly affect the performance.[1–7] For example, it has been observed that the vibratory power flow into the support base is directly related to its mobility[1–5] and the mobilities of the source and path, as well.[2,3] It has also been determined that power flow for the general isolator configuration is multi-dimensional including translational force and rotational moment coupling paths.[1,4–6] In fact, coupling mobility functions between these paths play a significant role in overall isolator performance.[5] Some investigators have shown that spectrally averaged behavior can be approximated for finite beam and platelike structures by replacing them with mobility expressions of corresponding infinite structures.[1–5] However, unique behavior at resonant conditions is then missed, especially near the first few system natural frequencies where peak power flow occurs.[3–6] Also, if active vibration isolation were to be attempted, lightly damped support base resonances with minimal modal overlap could have a detrimental effect on the stability of feedback control schemes.[7]

In compliant base (receiver) problems, the most appropriate measure with which to define isolation from a source to the receiver is vibratory power flow which accounts for both force and motion characteristics.[1–6] However, the problem of determining vibratory power flow through a *nonlinear* isolator path to a compliant, linear receiver is more complex. Here, the relationship between path and receiver mobilities can be excitation amplitude dependent and the dynamic response may have a wide spectral content, even for harmonic excitation.[8] Consequently, significant vibratory energy transmission may occur in a critical audio frequency range, even if the excitation source contains only lower-frequency components. Additionally, it is computationally difficult to analyze the complete system including the nonlinear path and compliant support base, especially when the base model is of high dimension. Traditionally, investigators have either focused on the localized nonlinear path while ignoring receiver dynamics or have resorted to a linear analysis of the complete system.

Compliant receiver problems commonly occur in vehicle applications where weight reduction for fuel efficiency consideration results in relatively flexible supporting frames.[9–11] It is also common to find that the isolation path between the excitation source and the compliant receiver contains significant, physically localized nonlinear elements.[12–14] As a practical illustration, consider the automotive hydraulic engine mount system of Fig. 1 which will serve as the primary example case in this article. A detailed cut-away of the mount is shown in Fig. 2. Construction details and other features may be found in the Ref. 13. Here, only vertical translational motion is being considered but the concepts introduced can easily be extended to the multi-

[a)]Corresponding Author Tel: (312) 413-7951, Fax: (312) 413-0447; Electronic mail: troyston@uic.edu

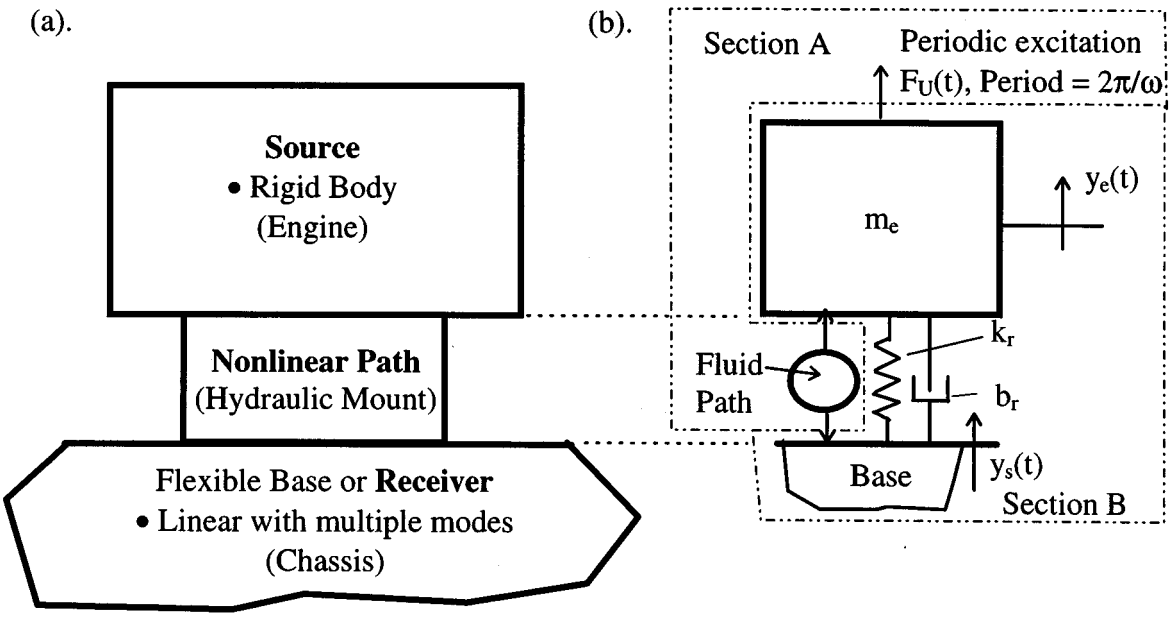

FIG. 1. Engine mount system.

dimensional case. The engine is assumed to be driven by a periodic vertical excitation force $F_U(t)$ of fundamental frequency ω, say representing imbalance forces. (Use of this simplistic model for unbalance force does have repercussions which will be discussed.) The engine is modeled as a rigid body and at the connection point to the mount, vertical motion is given by y_e. The vehicle chassis or support base is modeled using a linear multi-degree-of-freedom (MDOF) formulation and vertical displacement at the connection point to the mount is denoted as y_s.

Robustly modeling the hydraulic mount for a wide range of operating conditions requires a nonlinear description for several of its dynamic characteristics.[12] Recent studies by Kim and Singh[13] and Colgate *et al.*[14] have specifically focused on the strong nonlinearities associated with the decoupler. Such studies have employed the direct time domain numerical integration method which obviously is time consuming and may not lead to much physical insight. Additionally, if one also wishes to understand the coupled interaction of the engine mount with a compliant receiver, one has the increasingly difficult task of simultaneously integrating numerous coupled differential equations.

A common method of experimentally assessing the mount's isolation performance has been via dynamic stiffness in the frequency domain.[12,14] Some articles, in the context of a simplified vehicle model, have also used accelerance, chassis acceleration, force transmissibility and other motion and force related frequency response criteria.[12,13] All of these descriptors essentially assume the system is linear and they intentionally ignore response at frequencies other than the primary excitation frequency based on the ''low-pass filter'' argument. If the nonlinearity is very localized in the isolation path and there is sufficient damping in the system, then other frequency components of its response, assumed to be at higher harmonics, could be attenuated by the inherent low-pass filtering effect of inertial systems. This implies that subharmonic behavior is not present.

It is clear that a more fundamental study of vibratory power flow through a nonlinear path into a resonant receiver is needed. The hydraulic engine mounting system is an appropriate and practical example of such a situation. In a recent article by the authors,[15] a computational strategy based on the Galerkin method was proposed for an efficient analysis of complex mechanical systems with local nonlinearities. In the present article, this approach is extended to the rigid body source—nonlinear isolation path—compliant receiver

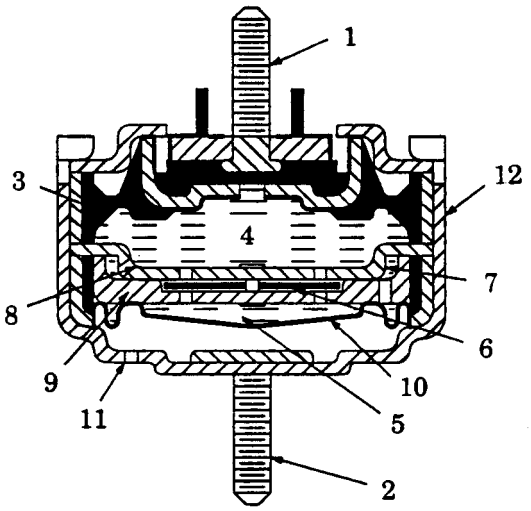

FIG. 2. Engine mount components. (1) and (2) mounting studs; (3) rubber which supports engine weight; (4) upper and (5) lower chambers filled with glycol fluid mixture; (6) decoupler; (7) inertia track; (8) upper and (9) lower plates which define decoupler gap; (10) lower chamber thin rubber bellow; (11) air breather; and (12) canister. See Kim and Singh (Ref. 13) for a more complete description.

TABLE I. Parameter values for engine mounting system.

$A_1=A_2=0.2726$ cm^2	$k_s=2\times10^4$ N/m	$p_{\text{atm}}=101.232$ kPa
$A_d=2.3\times10^{-3}$ m^2	$l_1=16.1$ cm, $l_2=5$ cm	$\rho_g=1.059\times10^{-3}$ kg/cm^3
$A_p=5.027\times10^{-3}$ m^2	$\eta_1=1.9\times10^{-3}$ kPa s^2/cm^3	$\overline{V_1}=0.715$ cm^3
$b_r=1000$ N s/m	$\eta_2=3.4\times10^{-3}$ kPa s^2/cm^3	$\overline{V_2}=28.251$ cm^3
$b_s=1400$ N s/m	$m_s=270$ kg	$\overline{V_{\text{air}}}=4$ cm^3
$C_{de}=0.65$	$m_e=122.7$ kg	$\omega_s=\sqrt{k_s/m_s}$
$k_r=2.7\times10^5$ N/m	$\overline{p}=116.4$ kPa	$\zeta_s=b_s/2\sqrt{k_s m_s}$

problem. The impact of ''softening'' the nonlinearity on predicted system response is investigated and isolation performance is assessed via calculation of total (multi-harmonic) vibratory power flow for harmonic excitation conditions. While the hydraulic engine mounting system serves as the primary example, the results should be conceptually applicable to many practical situations. Nonetheless, one must recognize that specific nonlinear path(s) must be carefully considered within the context of a system problem as illustrated in this article.

I. SYSTEM EQUATIONS

The physical system and theoretical model described below are based on papers co-authored by Kim and Singh[12,13] covering theoretical and experimental studies of production-grade hydraulic mounts. For periodic excitation at frequency ω, system response is assumed to be periodic with superharmonic content up to the N_pth order and subharmonic content up to the N_bth order. Kim and Singh's model was only experimentally validated for excitation frequencies below 50 Hz and this limitation is obeyed here. Equations are written as a function of the nondimensional time variable $\tau=\omega t/N_b$ or in terms of their frequency response at $\omega_n'=n\omega/N_b$, $n=1,\ldots,N_bN_p$. Governing equations are defined around static equilibria; hence, the static (gravitational) force is not present in the following formulation. Stiffness and damping elements, k_r and b_r, respectively, account for the rubber portion of the mount. They are shown schematically in Fig. 1. They are moderately nonlinear and are typically given as frequency-dependent parameters. Nominal values are provided in Table I. Since their amplitude dependence is minimal, the force associated with the mount rubber at a particular response frequency ω_n' can be expressed as follows where $j=\sqrt{-1}$:

$$F_r(\omega_n')=\left[j\,\frac{\omega_n'}{N_b}\,b_r(\omega_n')+k_r(\omega_n')\right][y_e(\omega_n')-y_s(\omega_n')]. \tag{1}$$

The fluid portion of the mount consists of upper and lower liquid-filled chambers connected via a large decoupler orifice and an inertia track. The inertia track refers to two relatively long and narrow fluid paths with significant inertial and damping properties. The inertia track acts as a vibration absorber tuned to the fundamental engine mounting resonance, providing inertia-augmented damping. For small amplitude excitation, the decoupler orifice is always open and essentially ''short circuits'' the inertia track. For larger amplitude motion, a plate in the decoupler orifice bottoms out and restricts flow for portions of the vibratory cycle, forcing fluid to flow through the inertia track.

The force from the fluid components acting on the engine and chassis is given by the following expression where A_p refers to the mount's equivalent fluid piston area, p_1 denotes its upper chamber fluid pressure, and $\overline{p}$ is the static equilibrium pressure in the fluid chambers:

$$F_f(\tau)=A_p[p_1(\tau)-\overline{p}]. \tag{2}$$

Newton's law applied to the engine mass, m_e, leads to the following:

$$\frac{\omega^2}{N_b^2}\,m_e\ddot{y}_e(\tau)=F_u(\tau)+F_f(\tau)-F_r(\tau). \tag{3}$$

First-order nonlinear differential equations describe the relationship between the pressure differential between the lower (2) and upper (1) fluid chambers and the resulting flow q_i through each inertia path, $i=1,2$:

$$\frac{N_b}{\omega I_i}\,[p_2(\tau)-p_1(\tau)]-\frac{\eta_i N_b}{I_i\omega}\,q_i(\tau)^2\ \text{sign}[q_i(\tau)]-\dot{q}_i(\tau)=0. \tag{4}$$

Here, $\dot{}$ denotes $d/d\tau$, $I_i=\rho_g l_i/A_i$ is the effective fluid inertia, and η_i is an experimentally measured fluid resistance parameter. Also, ρ_g refers to the mount fluid density, l_i denotes the ith inertia track length, and A_i is ith inertia track cross-sectional area. Flow through the decoupler orifice q_d is given by a similar nonlinear first-order differential equation:

$$\frac{N_b}{\omega I_d}\,[p_2(\tau)-p_1(\tau)]-\frac{\eta_d(\tau)N_b}{\omega I_d}\,q_d(\tau)^2\ \text{sign}[q_d(\tau)]-\dot{q}_d(\tau)=0, \tag{5}$$

where the expression for η_d is based on a turbulent flow assumption:

$$\eta_d(\tau)=\left(\frac{1}{C_{de}A_{de}(\tau)}\right)^2\frac{\rho_g}{2}, \tag{6}$$

with C_{de} denoting the discharge coefficient and $A_{de}(\tau)$ denoting the effective decoupler area. A kinematic model of the decoupler behavior is as follows. In the decoupled state, $A_{de}(\tau)=A_d$, and in the coupled state, $A_{de}(\tau)=0$, i.e., $q_d(\tau)=0$. The total volume flow through the decoupler orifice is denoted as v_d. Thus, we have $\dot{v}_d(\tau)=q_d(\tau)$. The decoupler free volume gap is given by $V_{\text{gap}}=A_d\Delta_d$, where Δ_d is the decoupler path length. At static equilibrium, the decoupler plate floats in the center. Hence, for $|v_d|\leqslant V_{\text{gap}}/2$ the decoupler plate does not block flow and $A_{de}(\tau)=A_d$. Under cyclic loading, starting from the equilibrium position, a positive pressure differential $[p_2(\tau)-p_1(\tau)]>0$ will result in an increase in $v_d(\tau)$. When $v_d(\tau)=V_{\text{gap}}/2$, $A_{de}(\tau)=0$ and hence v_d will not exceed $V_{\text{gap}}/2$. When the direction of flow reverses and $[p_1(\tau)-p_2(\tau)]<0$, the decoupler plate becomes unseated and again $A_{de}(\tau)=A_d$ until $v_d(\tau)=-V_{\text{gap}}/2$, at which time $A_{de}(\tau)=0$. As the flow reverses again, the process repeats itself. The effective orifice area can be expressed logically as follows: $A_{de}(\tau)=A_d$ if $|v_d|\leqslant V_{\text{gap}}/2$ or $v_d[p_1-p_2]>0$. Otherwise, $A_{de}(\tau)=0$. The

total flow between the two fluid chambers is given by the following first-order linear differential equation:

$$\frac{N_b}{\omega}(q_1(\tau)+q_2(\tau)+q_d(\tau))-\dot{v}(\tau)=0, \tag{7}$$

where v represents increments in the upper and lower chamber volumes from the $p_1=p_2=\overline{p}$ condition. The remaining equations relating pressure and volume in this lumped parameter fluid model are given below[12]

$$p_2(\tau)=5.26\times10^{-3}V_2(\tau)^{2.5}-8.9\times10^{-8}V_2(\tau)^6 + 1.41\times10^{-8}V_2(\tau)^{6.5}+p_{\text{atm}}, \tag{8a}$$

$$p_1(\tau) = \begin{cases} -6.4\overline{V_1}(\tau)+29.2V_1(\tau)^{7/6}+p_{\text{atm}}, & V_1(\tau)\geqslant 0, \quad (8b)\\ p_{\text{atm}}\overline{V}_{\text{air}}/(\overline{V}_{\text{air}}+|V_1(\tau)|), & V_1(\tau)<0, \quad (8c)\end{cases}$$

$$V_1(\tau)=\overline{V_1}+v(\tau)-A_p[y_e(\tau)-y_s(\tau)],$$
$$V_2(\tau)=\overline{V_2}-v(\tau). \tag{8d}$$

Here, V_1 and V_2 denote the hydraulic engine mount upper and lower fluid chamber volumes, respectively, p_{atm} denotes atmospheric pressure, and V_{air} is the air volume trapped in the upper fluid chamber.

For the engine and chassis, regardless of the number of degrees of freedom used to model them, the relationship between the force and motion at the interface to the fluid components of the mount can always be expressed as a transfer function in the frequency domain. The mount rubber dynamics can also be expressed this way. Consider harmonic motion of frequency ω_n'. Then, we will have harmonic displacement and force response at these connection points of the following form where $\sim$ denotes a complex-valued amplitude:

$$y_e(\tau)=\tilde{y}_e e^{j\omega_n'\tau}, \tag{9a}$$

$$y_s(\tau)=\tilde{y}_s e^{j\omega_n'\tau}, \tag{9b}$$

$$F_e(\tau)=\tilde{F}_e e^{j\omega_n'\tau}, \tag{9c}$$

$$F_s(\tau)=\tilde{F}_s e^{j\omega_n'\tau}. \tag{9d}$$

Consequently, a transfer function in the frequency domain between displacement and force at the connection points to section (A) of Fig. 1(b) can be written as such.

$$\tilde{\mathbf{T}}(\omega_n')=\begin{bmatrix} \dfrac{\tilde{y}_e}{\tilde{F}_e} & \dfrac{\tilde{y}_e}{\tilde{F}_s} \\ \dfrac{\tilde{y}_s}{\tilde{F}_e} & \dfrac{\tilde{y}_s}{\tilde{F}_s} \end{bmatrix}. \tag{10}$$

For the simplest case, where the engine mass is assumed to be rigid and the chassis is modeled as a single-degree-of-freedom (SDOF) linear system, we have the following expression, where m_s, b_s, and k_s denote the mass, linear viscous damping coefficient, and stiffness coefficient of the chassis:

$$\tilde{\mathbf{T}}(\omega_n')=\begin{bmatrix} k_r(\omega_n')-\omega_n'^2 m_e+j\omega_n' b_r(\omega_n') & -k_r(\omega_n')-j\omega_n' b_r(\omega_n') \\ -k_r(\omega_n')-j\omega_n' b_r(\omega_n') & k_r(\omega_n')+k_s-\omega_n'^2 m_s+j\omega'[b_r(\omega_n')+b_s] \end{bmatrix}. \tag{11}$$

II. MODELING AND COMPUTATIONAL STRATEGIES

A. Modeling issues

If the single-degree-of-freedom receiver model is used, it is fairly straightforward to analyze the system response using the direct time numerical integration technique. The system is composed of four first-order and two second-order differential equations. Of course, the mount rubber nonlinearity, which is defined in the frequency domain, must be approximated; but this is one of the weaker nonlinearities. For more complex support structure models where many degrees of freedom are considered, numerical integration will become very complex and inefficient. In a previous article, a solution method for complex systems with local nonlinearities was developed.[15] The method is based on the Galerkin procedure and employs order reduction to reduce the number of degrees of freedom to be solved using an iterative strategy, and continuation to aid in parametric studies. The advantage of the method is that complex linear receiver models of many degrees of freedom, either based on theory or experimental transfer function data, are easily incorporated with minimal additional cost in solution time.

Several difficulties are encountered when trying to solve the decoupler-equipped, multi-path inertia track equations using the Galerkin procedure. Explicit differentiable analytical expressions are needed. An approximation for the logic-based decoupler equations is proposed here based on physical reasoning. If there is any compliance in the decoupler orifice plate or the mechanical stops, one should approximate its force versus position relationship as a spring with a backlash or deadspace regime and stiffness k_d. In general, piecewise discontinuity in the Galerkin code is tolerable. But if the degree of nonlinearity is very high, many frequency components are needed in the periodic solution. A further approximation using a polynomial stiffness expression can be more easily handled and is given as follows where γ refers to the order of the polynomial:

$$F_d=k_d(2v_d/A_d\Delta_d)^{\gamma}. \tag{12}$$

Urabe and Reiter[16] formulated the Galerkin procedure for either first- or second-order differential equations. The

hydraulic mounting system model, excluding base dynamics, consists of four first-order differential equations for the fluid processes and one second-order differential equation for the mount rubber/engine mass degree of freedom. While, both first- and second-order differential equations can be simultaneously handled using the procedure, some modifications are proposed for the sake of computational efficiency. Additionally, direct calculation of v_d is needed to implement Eq. (12).

Two first-order differential equations representing the volume of fluid flow through a single inertia track may be cascaded to obtain one second-order differential equation. This reduces the complexity of the Galerkin implementation since the order of the problem (in terms of the sizes of arrays that must be handled) is the same for each additional first- or second-order equation. However, representing the total fluid volume flow through each path with a second-order differential equation results in an unrestrained degree of freedom. While the ''spring'' force of the decoupler acts to restore the total flow through it to zero, no such force is applied on either inertia path. Consequently, total volume flow through either inertia path is unrestrained, which allows a nonzero mean circulating fluid flow. While this condition has little consequence in the physical system dynamics, it is a source of numerical instability in the Galerkin method. To remedy this difficulty, it is proposed to approximate the two in-parallel inertia paths ($i=1,2$) with one equivalent path (e) using the following dynamic relationships:

$$\eta_e=\frac{\eta_1\eta_2}{(\sqrt{\eta_1}+\sqrt{\eta_2})^2}, \tag{13a}$$

$$I_e=\rho_g l_e/A_e, \tag{13b}$$

$$l_e=l_1 l_2/(l_1+l_2), \tag{13c}$$

$$A_e=A_1=A_2. \tag{13d}$$

This further reduces the equations for the fluid processes to only two degrees of freedom with nonlinearities defined in the time domain which are given as follows:

$$\frac{N_b^2}{\omega^2 I_e}[p_2(\tau)-p_1(\tau)]-\frac{\eta_e}{I_e}\dot{v}_e(\tau)^2\ \mathrm{sign}[\dot{v}_e(\tau)]-\ddot{v}_e(\tau)=0, \tag{14a}$$

$$\frac{N_b^2}{\omega^2 I_d}[p_2(\tau)-p_1(\tau)]-\frac{\eta_d}{I_d}\dot{v}_d(\tau)^2\ \mathrm{sign}[\dot{v}_d(\tau)]-\frac{N_b^2}{\omega^2 I_d}F_d(\tau)-\ddot{v}_d(\tau)=0. \tag{14b}$$

B. Computational method

With the above modifications, application of the Galerkin strategy is briefly reviewed. As indicated in Fig. 1(b), the system can be divided into two sections, (A) and (B). Section (A), comprising the fluid components of the mount, contains the $N_v=2$ second-order differential equations (14a) and (14b) with nonlinearities defined in the time domain. These two expressions are the determining equations, $\mathbf{d}^v(\tau)$, for the Galerkin method. Section (B), the engine, chassis and rubber components of the mount, consists of N_w linear differential equations as well as equations with nonlinearities defined in the frequency domain. These N_w equations will be dependent on the displacement vector $\mathbf{w}$ or state variables in section (B). This section can be analyzed completely in the frequency domain using linear algebraic methods. The connection between section (B) and section (A), as indicated above, is described by the vector $\mathbf{y}(\tau)\equiv[y_e(\tau)y_s(\tau)]^T$ which is a linear mapping of $\mathbf{w}(\tau)$. Here, superscript T denotes the transpose. Likewise, the force vector at this connection is described by an $N_y=2$ dimensional vector $\mathbf{F}_y(\tau)\equiv[F_e(\tau)F_s(\tau)]^T$. Hence, for section (B), a frequency-dependent transfer function may be defined as follows:

$$\tilde{\mathbf{T}}_{\mathbf{y}}(\omega')\equiv\frac{\tilde{\mathbf{y}}}{\tilde{\mathbf{F}}_{\mathbf{y}}}(\omega'). \tag{15}$$

Now, the N_bN_pth approximate solution to the problem will have the following form:

$$\mathbf{v}(\tau)=\mathbf{a}_0^v+\sum_{n=1}^{N_bN_p}\mathbf{a}_{2n-1}^v\sin(n\tau)+\mathbf{a}_{2n}^v\cos(n\tau),$$

$$\mathbf{v}\equiv[v_e,v_d]^T,\quad \mathbf{a}_n^v\equiv[a_n^{v_e},a_n^{v_d}]^T, \tag{16a}$$

$$\mathbf{y}(\tau)=\mathbf{a}_0^y+\sum_{n=1}^{N_bN_p}\mathbf{a}_{2n-1}^y\sin(n\tau)+\mathbf{a}_{2n}^y\cos(n\tau),$$

$$\mathbf{y}\equiv[y_e,y_s]^T,\quad \mathbf{a}_n^y\equiv[a_n^{y_e},a_n^{y_s}]^T. \tag{16b}$$

By substituting expressions (16a) and (16b) into Eqs. (14a) and (14b) and numerically calculating the Fourier coefficients of $\mathbf{d}^{\mathbf{v}}(\tau)$, we obtain the following $(4N_bN_p+1)\times(N_v)$ nonlinear algebraic determining equations for finding the values of the coefficients

$$\boldsymbol{\alpha}^v\equiv[\mathbf{a}_0^v\ \ \mathbf{a}_1^v\ \ \cdots\ \ \mathbf{a}_{4N_bN_p}^v]$$

and

$$\boldsymbol{\alpha}^y\equiv[\mathbf{a}_0^y\ \ \mathbf{a}_1^y\ \ \cdots\ \ \mathbf{a}_{4N_bN_p}^y]:$$

$$\mathbf{D}_i^v(\boldsymbol{\alpha})\equiv\mathscr{T}_i[\mathbf{d}^v(\tau)]=\mathbf{0},\quad i=0,\ \ldots,4N_bN_p,$$

where

$$\boldsymbol{\alpha}\equiv[\boldsymbol{\alpha}^v\ \ \boldsymbol{\alpha}^y]^T,\quad \mathscr{T}_0[d(\tau)]\equiv\frac{1}{2N_f}\sum_{n_f=1}^{2N_f}d(\tau_{n_f}),$$

$$\mathscr{T}_{2n-1}[d(\tau)]\equiv\frac{1}{N_f}\sum_{n_f=1}^{2N_f}d(\tau_{n_f})\sin(n\tau_{n_f}),$$

$$\mathscr{T}_{2n}[d(\tau)]\equiv\frac{1}{N_f}\sum_{n_f=1}^{2N_f}d(\tau_{n_f})\cos(n\tau_{n_f}),$$

$$n=1,\ \ldots,2N_bN_p,$$

and

$$\tau_{n_f}=\frac{2n_f-1}{2N_f}\pi\ \text{ with }\ N_f\geqslant 2N_bN_p,\ n_f=1,\ \ldots,N_f. \tag{17}$$

The remaining $(4N_bN_p+1)\times(N_y)$ determining equations which are needed take the following form. Here, Re and Im

refer to the real and imaginary parts, respectively:

$$D_0^{y_r}(\boldsymbol{\alpha}) \equiv \sum_{z=1}^{N_y} \{\mathrm{Re}[\tilde{T}_y^{r,z}(0)] a_0^{F_z}\} - a_0^{y_r} = 0, \tag{18a}$$

$$D_{2n-1}^{y_r}(\boldsymbol{\alpha}) \equiv \sum_{z=1}^{N_y} \left\{ \mathrm{Re}\left[\tilde{T}_y^{r,z}\left(\frac{n\omega}{N_b}\right)\right] a_{2n-1}^{F_z} + \mathrm{Im}\left[\tilde{T}_y^{r,z}\left(\frac{n\omega}{N_b}\right)\right] a_{2n}^{F_z} \right\} - a_{2n-1}^{y_r} = 0, \tag{18b}$$

$$D_{2n}^{y_r}(\boldsymbol{\alpha}) \equiv \sum_{z=1}^{N_y} \left\{ \mathrm{Re}\left[\tilde{T}_y^{r,z}\left(\frac{n\omega}{N_b}\right)\right] a_{2n}^{F_z} - \mathrm{Im}\left[\tilde{T}_y^{r,z}\left(\frac{n\omega}{N_b}\right)\right] a_{2n-1}^{F_z} \right\} - a_{2n}^{y_r} = 0, \tag{18c}$$

where $r=1,\ldots,N_y$, $n=1,\ldots,2N_bN_p$ and

$$a_i^{F_z} \equiv \mathscr{F}_i[F_z(\tau)], \quad i=0,\ldots,4N_bN_p.$$

Consequently, using this order reduction technique, the number of coupled nonlinear algebraic equations to be iteratively solved remains fixed at $N=(N_y+N_v)\times(4N_bN_p+1)$ regardless of the number of equations N_w describing motion in section (B). Once the nonlinear solution is obtained, the response of any variable in section (B) is quickly found by simple linear algebraic calculations.

The Galerkin method employs an iterative method to solve the coupled nonlinear algebraic equations, minimizing the sum of the squares of the determining equations in the frequency domain (a least squares approach). Further details of the method can be found in Refs. 15 and 16.

C. Power flow computation

Assuming a periodic response with fundamental frequency ω/N_b, the spectral content of vibratory power flow throughout the system may be calculated from the Galerkin procedure results. For a given dynamic displacement variable $z(\tau)$, there is an associated constraint force variable $F_z(\tau)$, both of which can be expressed in the following series forms:

$$z(\tau) = a_0^z + \sum_{n=1}^{N_bN_p} a_{2n-1}^z \sin(n\tau) + a_{2n}^z \cos(n\tau), \tag{19a}$$

$$F_z(\tau) = a_0^{F_z} + \sum_{n=1}^{N_bN_p} a_{2n-1}^{F_z} \sin(n\tau) + a_{2n}^{F_z} \cos(n\tau). \tag{19b}$$

The associated vibratory power flow can then be formulated from the inner product of the force and velocity by summing respective harmonic contributions:

$$P(\omega) = \sum_{n=1}^{N_bN_p} \frac{n\omega}{2N_b} [-a_{2n-1}^{F_z} a_{2n}^z + a_{2n}^{F_z} a_{2n-1}^z]. \tag{20}$$

For example, vibratory power flow through the mount into the automotive chassis will be given by Eqs. (19) and (20) where

$$F_z(\tau) = F_r(\tau) - F_f(\tau), \quad a_i^{F_z} \equiv \mathscr{F}_i[F_z(\tau)],$$

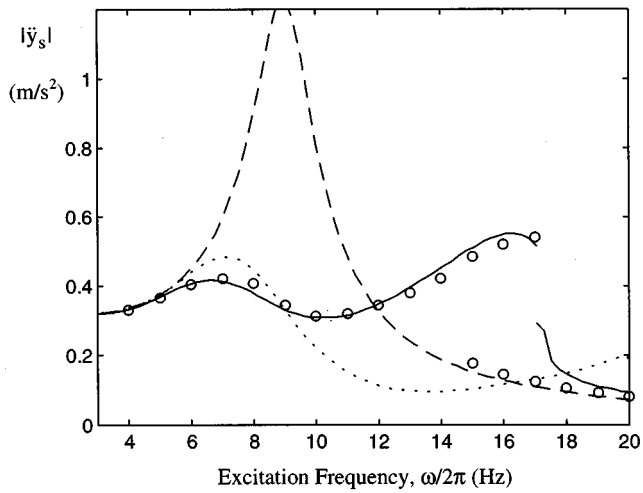

FIG. 3. Mounting system frequency response. Base acceleration at the excitation frequency, $\ddot{y}_s(\omega)$, for, $F_u(t)=100\sin(\omega t)N$. Key: – – – rubber mount (modal method), - - - - inertia mount with no decoupler, $\Delta_d=0$ mm (Galerkin solution and numerical integration), ∘∘∘ kinematic decoupler model, $\Delta_d=0.7$ mm (numerical integration), — polynomial-stiffness decoupler model with $\gamma=3$, $\Delta_d=0.7$ mm (Galerkin solution and numerical integration).

and (21)

$$a_i^z = a_i^{y_s}.$$

Vibratory power flow through the rubber component or the fluid component of the mount may be considered separately by using $F_z(\tau)=F_r(\tau)$ or $F_z(\tau)=-F_f(\tau)$, respectively.

III. RESULTS AND DISCUSSION

A. Improvement in mount models

In the previous section, modifications to the vibration mount model were proposed to make the problem tractable using the Galerkin method. The impact of these changes is assessed via comparison of the modified case to the exact kinematic case for harmonic excitation using the SDOF base model. System parameter values used in this study are provided in Table I. These values are based on experimental studies of a typical commercially used engine mount system. In Fig. 3, base acceleration $\ddot{y}_s$ at the fundamental harmonic of the excitation force $F_U(t)=100\sin(\omega t)N$ for $3<\omega/2\pi<20$ Hz is shown for the kinematic and polynomial-stiffness decoupler models. This range of excitation values represents realistic conditions. Also shown is the system response using the rubber mount alone (excluding fluid elements) and using the inertia track mount which does not possess a decoupler, i.e., $\Delta_d=0$. Results of Fig. 3 bear much similarity to comparable cases reported in Fig. 9a of Kim and Singh[13] supporting the validity of the equivalent inertia track formulation. The superiority of the highly nonlinear decoupler-equipped mount is evident from the fact that it allows the inertia track to act like a tuned absorber at the engine mounting resonance, attenuating the otherwise large peak near $\omega/2\pi=10$ Hz, but then it decouples the track as the frequency is increased for reduced motion transmissibility.

The two decoupler models agree fairly well over this frequency range. A hardening stiffness effect associated with

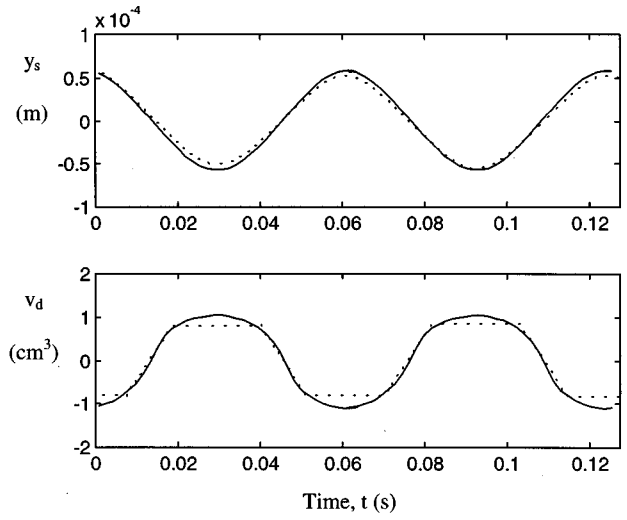

FIG. 4. Mounting system time response. Base motion, $y_s(t)$, and the total volume flow through the decoupler orifice, $v_d(t)$, for $\Delta_d=0.7$ mm and $F_u(t)=100\sin(15.86\times 2\pi t)N$ (large amplitude solution). Key - - - - kinematic decoupler model (numerical integration), — polynomial-stiffness decoupler model with $\gamma=3$ (Galerkin solution and numerical integration).

the decoupler is evident in both cases as the system resonance has the characteristic upward bend in frequency.[17] For the kinematic model with the stronger nonlinearity, a jump phenomenon is also observed with multiple solution regimes. The weaker polynomial-stiffness model did not predict a strong jump phenomenon, but did have a region of numerical difficulty where a solution, either stable or unstable, could not be found with the Galerkin method. Hence, there is a break in the solution path.

In Fig. 4, selected time domain plots of the decoupler total volume displacement v_d and the base motion y_s are provided to illustrate the following points. First, the ''low-pass filter effect'' is evident as high-frequency motion of the base is significantly curtailed. In other words, the sharp discontinuities in v_d are not evident in y_s. Second, it is clear that ''softening'' the decoupler model, i.e., weakening the path nonlinearity, also lowers the high-frequency response of the system. The solid line in Fig. 4b, based on the ''softened'' model, is smoother. In Fig. 5, this same trend is observed where fundamental and higher harmonic responses to harmonic excitation are shown for the kinematic and polynomial-stiffness decoupler models. Neither model predicted any significant subharmonic response. Results shown here also raise questions with respect to how nonlinear isolation performance should be assessed. Clearly, it seems that ignoring the system response at frequencies other than the excitation frequency may be inappropriate. This issue is addressed in the next section.

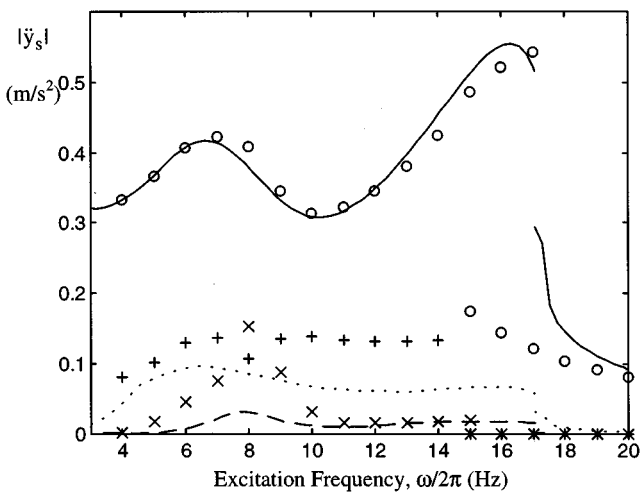

FIG. 5. Mounting system frequency response. Base acceleration at the excitation frequency and its first two harmonics, $\ddot{y}_s$, for $\Delta_d=0.7$ mm and $F_u(t)=100\sin(\omega t)N$. Key: Kinematic decoupler model, ∘∘∘ 1st, ××× 2nd, +++ 3rd harmonics (numerical integration), polynomial-stiffness decoupler model with $\gamma=3$, — 1st, – – 2nd, - - - - 3rd harmonics (Galerkin solution and numerical integration).

B. Vibratory power flow

Using Eqs. (19)–(21), several vibratory power flow variables are calculated and graphed in Fig. 6 for the different

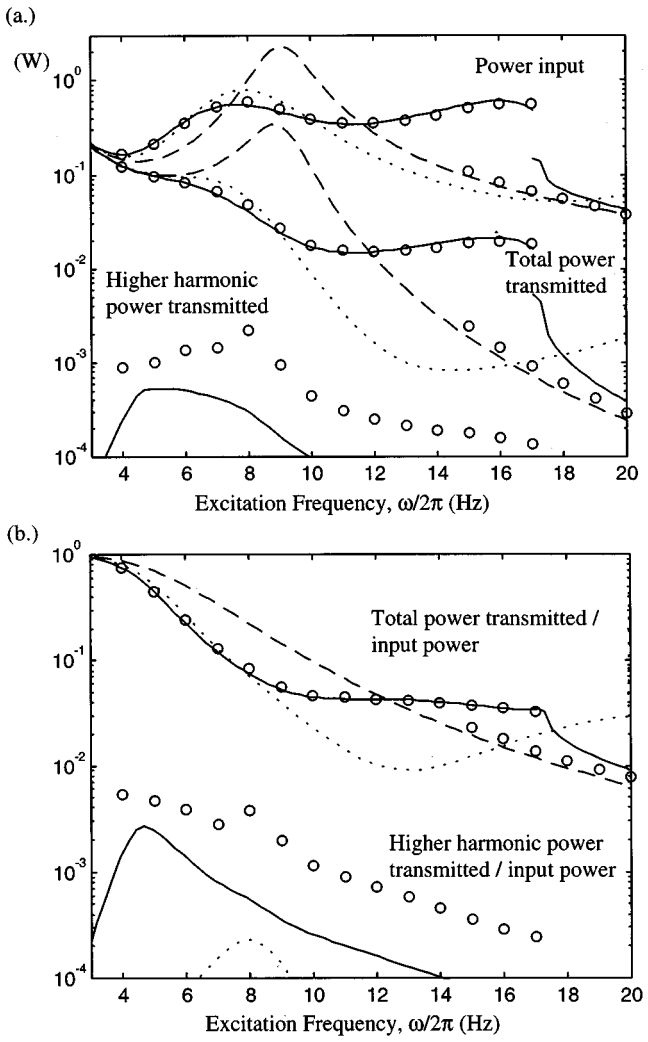

FIG. 6. Mounting system frequency response. Vibratory power flow for different mount models. (a) Power input, total and higher harmonic power transmission into support base. (b) Ratio of total and higher harmonic power transmission to power input. Here, $F_u(t)=100\sin(\omega t)N$. Key: – – – rubber mount (modal method), - - - - inertia mount with no decoupler, $\Delta_d=0$ mm (Galerkin solution and numerical integration), ∘∘∘∘ kinematic decoupler model $\Delta_d=0.7$ mm (numerical integration), — polynomial-stiffness decoupler model with $\gamma=3$, $\Delta_d=0.7$ mm, (Galerkin solution and numerical integration).

decoupler configurations and models. Power related quantities are also provided in Table II. Directions of positive vibratory power flow in Fig. 7 show that the fluid component of the engine mount absorbs vibratory energy at the excitation frequency coming from both the engine (source) and the chassis (receiver). However, it also acts as a source of vibratory energy at higher frequencies which is then transmitted and dissipated throughout the rest of the system. Vibratory power results support the conclusion based on motion descriptor analysis that the ''softened'' nonlinear decoupler model does predict less vibration transmission at higher frequencies than is predicted by the kinematic decoupler model.

Results also show that, on a quantitative basis, the contribution to the total vibratory energy transmission of the higher harmonic components is negligible with respect to the primary harmonic, supporting performance assessment methods based on the ''low-pass filter'' assumption in this particular case. This fact must however, be qualified by two remarks. First, the frequency of transmission in addition to its level is of interest. Results reported here indicate that, even for source excitation below 20 Hz, structure-borne noise is transmitted through the mount in the audible frequency range. Even if the relative energy is low, its perceived level in terms of radiated sound in, for example, the passenger compartment may still be significant. Second, in this example case, the base is a simplistic, SDOF model, with a 40 dB/decade attenuation in the mobility spectrum above its resonance frequency near 1.36 Hz. Other base models with reduced frequency attenuation or high-frequency resonant conditions may lead to different conclusions. This is discussed in the next section.

C. MDOF resonant receivers

Due to computational difficulty, most prior studies of isolation systems with localized mount nonlinearities have typically either focused on the mount alone and ignored complex support base dynamics or have resorted to a linear analysis of the complete system. Here, using the Galerkin-based computational strategy, both path nonlinearities and more realistic, MDOF receiver dynamics are considered. Several generic receiver models are considered for evaluation of their impact on system performance. They include the

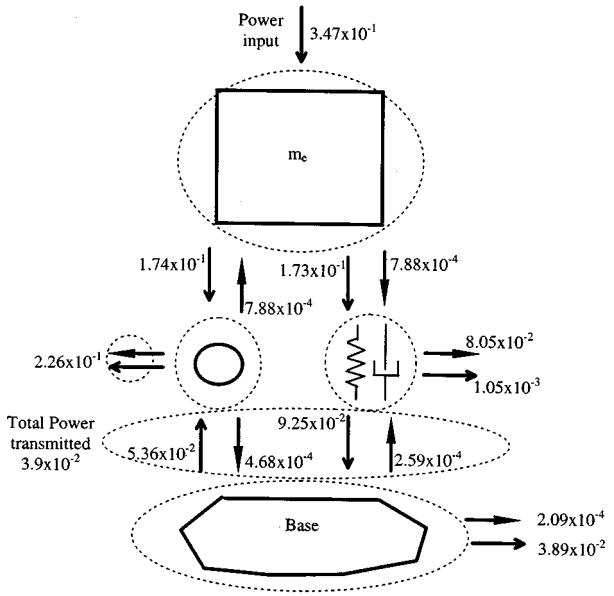

FIG. 7. Mounting system schematic showing directions of positive vibratory power flow for the SDOF base model and the polynomial-stiffness decoupler model with $\gamma=3$. Key: → primary harmonic, → higher harmonics.

SDOF base used in the previous sections, a purely viscous damper base, a MDOF base with heavy modal damping comparable to that of the SDOF base, and a more lightly damped MDOF base. Mobilities for each of these bases are given by the following equations:

SDOF base:

$$\frac{\tilde{y}_s}{\tilde{F}_s}(\omega_n')=\frac{1}{k_s}\frac{j\omega_n'}{(1-(\omega_n'/\omega_s)^2)+j(2\varsigma_s\omega_n'/\omega_s)}. \tag{22}$$

Pure viscous damper base:

$$\frac{\tilde{y}}{\tilde{F}_s}(\omega_n')=\frac{1}{b_s}. \tag{23}$$

MDOF heavily damped base:

TABLE II. Vibratory power flow for different mount models. Given SDOF base of Eq. (22).

Power quantity[a] (Watts)	Rubber mount (linear system)	Inertia track without decoupler	With inertia track and decoupler $\Delta_d=0.7$ mm	
			Kinematic model	Poly-stiffness model, $\gamma=3$
Power input				
primary harmonic only	0.398	0.244	0.341	0.347
Power transmitted to Base				
primary harmonic	8.60×10^{-2}	3.55×10^{-2}	4.01×10^{-2}	3.89×10^{-2}
(% of TOTAL)	(100)	(99.9)	(98.5)	(99.5)
superharmonics	0	2.65×10^{-5}	5.93×10^{-4}	2.08×10^{-4}
(% of TOTAL)	(0)	(0.1)	(1.5)	(0.5)
TOTAL	8.60×10^{-2}	3.55×10^{-2}	4.07×10^{-2}	3.91×10^{-2}
(% of power input)	(21.6)	(14.5)	(11.9)	(11.3)

[a]Averaged over $3<\omega/2\pi<20$ Hz.

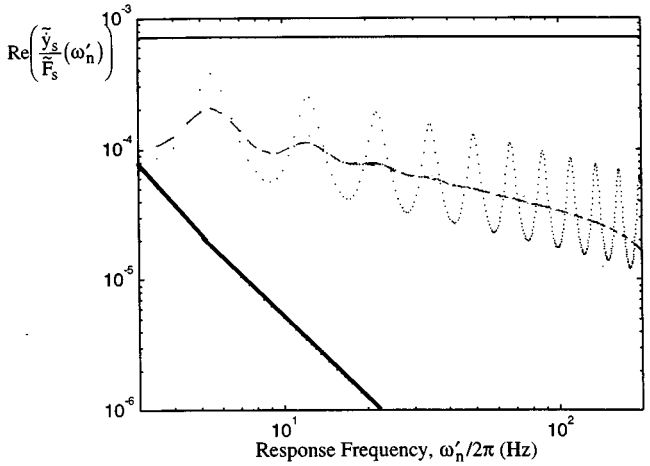

FIG. 8. Mobility of base models. Key: — SDOF base, Eq. (22), — viscous damper base, Eq. (23), – – MDOF heavily damped base, Eq. (24), ···· MDOF lightly damped base; Eq. (25).

$$\frac{\tilde{\ddot{y}}_s}{\tilde{F}_s}(\omega_n')=\sum_{i=1}^{12}\frac{1}{i^4 k_s}\frac{j\omega_n'}{(1-(\omega_n'/i^2\omega_s)^2)+j(2\varsigma_s\omega_n'/i^2\omega_s)}. \tag{24}$$

MDOF lightly damped base:

$$\frac{\tilde{\ddot{y}}}{\tilde{F}_s}(\omega_n')=\sum_{i=1}^{12}\frac{1}{i^4 k_s}\frac{j\omega_n'}{(1-(\omega_n'/i^2\omega_s)^2)+j(2\varsigma_s\omega_n'/i^3\omega_s)}. \tag{25}$$

The real part of their mobilities is shown in Fig. 8 since it is proportional to the level of vibratory power transmission from a force applied directly to the support base point, y_s.[1] As seen in the log–log plot, the SDOF base has a mobility that is attenuated at a rate of 40 dB/decade above its resonance frequency. Thus, it is operated almost entirely in the inertia-driven regime. The mobility of a pure viscous damper is constant with respect to frequency. The mobilities of the MDOF bases are more complex, particularly for the lightly damped base, but follow a mean attenuation trend with frequency that lies somewhere in-between the SDOF and the viscous damper cases.

Vibratory power flow through the mount into the SDOF support base is shown in Fig. 9. Vibratory power flow for the cases of the pure viscous damper base, MDOF heavily damped base, and MDOF lightly damped base are shown in Figs. 10, 11, and 12, respectively. Some numerical values are also given in Table III. Several observations can be made. First, with the SDOF base, the highest levels of power dissipation in the mount are obtained. This is because excitation is well above the base natural frequency which acts as a mass barrier with a high impedance, or equivalently a low mobility, for power transmission.

Second, for the viscous damper, a greater ratio of power flow to input power occurs due to the relative higher mobility, i.e., lower impedance, of the base as frequency increases. Increasing the level of damping in the base, i.e., lowering the mobility, does decrease the level of transmission. Note also that, for the viscous damper base, the level of vibratory input has been significantly decreased. Changing the mobility of

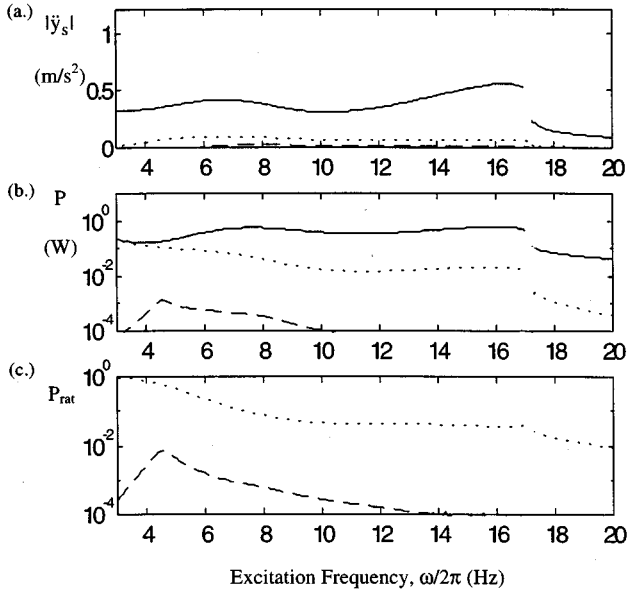

FIG. 9. Mounting system frequency response. Vibratory power flow into the SDOF support base (Polynomial-stiffness decoupler model with $\gamma=3$, Galerkin solution). Here, $F_u(t)=100\sin(\omega t)N$ and $\Delta_d=0.7$ mm. (a) Base vertical acceleration, $\ddot{y}_s$, — 1st harmonic, – – 2nd harmonic, - - - - 3rd harmonic. (b) Power transmission, — Power input, - - - - Total power transmitted, – – Power transmitted at higher harmonics. (c) Power transmission ratios, - - - - Total power transmitted/Power input, – – Power transmitted at higher harmonics/ Power input.

the base also changes the mobility at the excitation drive point. This brings up the point that a force input alone is often not a true representation of dynamic engine imbalance or other practical sources of vibration excitation. Other in-

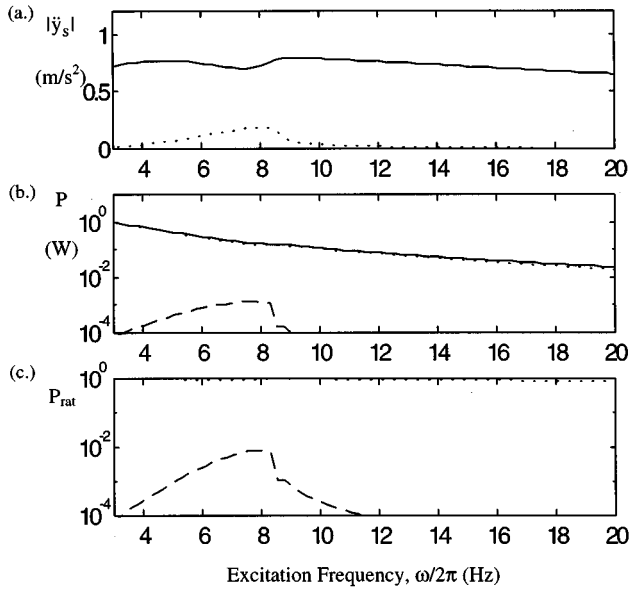

FIG. 10. Mounting system response. Vibratory power flow into the pure viscous damper base (Polynomial-stiffness decoupler model with $\gamma=3$, Galerkin solution). Here, $F_u(t)=100\sin(\omega t)N$ and $\Delta_d=0.7$ mm. (a) Base vertical acceleration, $\ddot{y}_s$, — 1st harmonic, – – 2nd harmonic, - - - - 3rd harmonic. (b) Power transmission, — Power input, - - - - Total power transmitted, – – Power transmitted at higher harmonics. (c) Power transmission ratios, - - - - Total power transmitted/Power input, – – Power transmitted at higher harmonics/Power input.

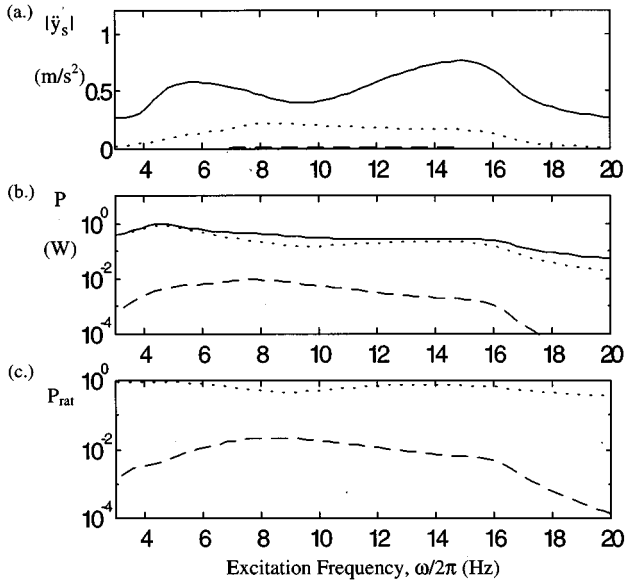

FIG. 11. Mounting system response. Vibratory power flow into the MDOF heavily damped support base (Polynomial-stiffness decoupler model with $\gamma=3$, Galerkin solution). Here, $F_u(t)=100\sin(\omega t)N$ and $\Delta_d=0.7$ mm. (a) Base vertical acceleration, $\ddot{y}_s$, — 1st harmonic, – – 2nd harmonic, - - - - 3rd harmonic. (b) Power transmission, — Power input, - - - - Total power transmitted, – – Power transmitted at higher harmonics. (c) Power transmission ratios, - - - - Total power transmitted/Power input, – – Power transmitted at higher harmonics/Power input.

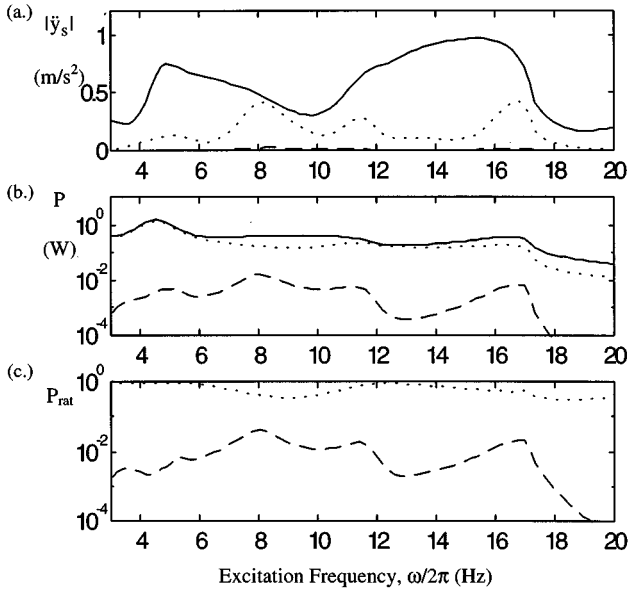

FIG. 12. Mounting system response. Vibratory power flow into the MDOF lightly damped support base (Polynomial-stiffness decoupler model with $\gamma=3$, Galerkin solution). Here, $F_u(t)=100\sin(\omega t)N$ and $\Delta_d=0.7$ mm. (a) Base vertical acceleration, $\ddot{y}_s$, — 1st harmonic, – – 2nd harmonic, - - - - 3rd harmonic. (b) Power transmission, — Power input, - - - - Total power transmitted, — — Power transmitted at higher harmonics. (c) Power transmission ratios, - - - - Total power transmitted/Power input, – – Power transmitted at higher harmonics/Power input.

puts, such as velocity or more complex ones which are dependent on the system response may be more suitable for a given application. In fact, it has been shown in previous linear system isolation studies on resonant support structures that force inputs will favor power transmission at resonances.[2,3] Since there are no such resonances for the viscous damper case in the frequency range of interest, power input is reduced.

Third, for the MDOF bases considered, regardless of the level of damping, a greater amount of vibratory power flows to the base than in the SDOF case since the mobility is significantly higher. Note also, that a greater percentage of the power transmission occurs at higher harmonics of the excitation frequency. For the lightly damped MDOF base, isolation performance is more frequency dependent. But, for both MDOF cases, even when the level of modal damping in the base is increased, while vibratory power transmission at specific frequencies may be attenuated, the overall level of transmission for wideband excitation is virtually unchanged. This has important practical implications, as it shows that added base damping (with more weight, of course) may not offer substantial gains in performance depending on the excitation conditions.

Finally, in Table III it is interesting to note that trends in the percentage of higher harmonic power flow do not match trends in the overall power flow which were easily related to trends in support base mobility. This is due to the mechanism of generating higher harmonics which is related to the mount nonlinearity and is highly amplitude dependent. Even though the pure viscous damper has a higher mobility, it does not produce large amplitude motion across the mount. Thus, while the percentage level of overall power flow may be well correlated with the level of base mobility, the generation and

TABLE III. Vibratory power flow for different base models ($\Delta_d=0.7$ mm, polynomial decoupler model with $k_d=10$ KPa and $\gamma=3$).

Power quantity[a] (Watts)	SDOF Eq. (22)	Viscous Eq. (23)	MDOF heavily damped. Eq. (24)	MDOF lightly damped. Eq. (25)
Power input				
primary harmonic only	0.347	0.176	0.349	0.360
Power transmitted to Chassis				
primary harmonic	3.89×10^{-2}	1.66×10^{-1}	2.45×10^{-1}	2.42×10^{-1}
(% of TOTAL)	(99.5)	(99.9)	(98.6)	(98.5)
superharmonics	2.08×10^{-4}	2.14×10^{-4}	3.53×10^{-3}	3.63×10^{-3}
(% of TOTAL)	(0.5)	(0.1)	(1.4)	(1.5)
TOTAL	3.91×10^{-2}	1.67×10^{-1}	2.49×10^{-1}	2.46×10^{-1}
(% of power input)	(11.3)	(94.9)	(70.2)	(68.7)

[a]Averaged over $3<\omega/2\pi<20$ Hz.

transmission of higher harmonic vibratory energy is dependent in a more complex way on the interactions between the support base dynamics and the mount dynamics.

IV. CONCLUSION

This study has made a number of contributions to the general understanding of vibratory power flow through a nonlinear isolator path into a resonant receiver with some particular insights into the hydraulic engine mounting system. An enhanced Galerkin method, a multi-term harmonic balance strategy, was used to solve for the steady-state periodic response and isolation performance was assessed in terms of total (multi-harmonic) vibratory power flow under harmonic excitation conditions.

Several key findings are reported, including the following. While modeling the isolation path with a ''softened'' nonlinear expression may only moderately alter the fundamental harmonic response, it can significantly alter higher harmonic responses. In some cases, these higher harmonic responses represent structure-borne noise which has been generated by subaudio frequency excitations. It has also been shown that compliant base (receiver) dynamics can significantly affect isolation performance. Use of a SDOF support structure produces superior performance relative to a MDOF base since the base mobility is less for the SDOF case. Also, for a MDOF base, significant levels of vibratory power flow may be transmitted at higher harmonics of the excitation frequency for a wide range of base damping levels. For spectrally averaged analysis, it is the mean level of mobility that is important at higher frequencies. This is somewhat independent of the modal damping level but dependent on the number of degrees of freedom. Finally, it has been shown that while overall levels of vibratory power flow are well correlated with support base mobility, the generation and transmission of higher harmonic power flow are more dependent on the coupled source—nonlinear path—receiver dynamics.

The study of nonlinear paths is a fertile ground for future research. For instance, issues which still need to be addressed include a careful consideration of vibratory power flow under multi-harmonic and other nonperiodic excitation conditions coming from both force and motion-type sources applied through multi-dimensional path configurations. Unlike linear systems, nonlinear system responses due to different excitation frequencies are not independent. Additionally, other MDOF receiver models representing typical applications, including those with structural damping as opposed to viscous damping, should be considered. These situations are currently being investigated by the authors.

[1] H. G. D. Goyder and R. G. White, ''Vibrational power flow from machines into built-up structures, Part I: Introduction and approximate analyses of beam and plate-like foundations,'' J. Sound Vib. **68**, 59–75 (1980).
[2] H. G. D. Goyder and R. G. White, ''Vibrational power flow from machines into built-up structures, Part III: Power flow through isolation systems,'' J. Sound Vib. **68**, 97–117 (1980).
[3] R. J. Pinnington and R. G. White, ''Power flow through machine isolators to resonant and non-resonant beams,'' J. Sound Vib. **75**, 179–197 (1981).
[4] Y. K. Koh and R. G. White, ''Analysis and control of vibrational power transmission to machinery supporting structures subjected to a multi-excitation system, Part I: Driving point mobility matrix of beam and rectangular plates,'' J. Sound Vib. **196**, 469–493 (1996).
[5] Y. K. Koh and R. G. White, ''Analysis and control of vibrational power transmission to machinery supporting structures subjected to a multi-excitation system, Part II: Vibrational power analysis and control schemes,'' J. Sound Vib. **196**, 495–508 (1996).
[6] J. Pan, J. Pan, and C. H. Hansen, ''Total power flow from a vibrating rigid body to a thin panel through multiple elastic mounts,'' J. Acoust. Soc. Am. **92**, 895–907 (1992).
[7] K. B. Scribner, L. A. Sievers, and A. H. von Flotow, ''Active narrowband vibration isolation of machinery noise from resonant substructures,'' J. Sound Vib. **167**, 17–40 (1993).
[8] T. J. Royston and R. Singh, ''Optimization of passive and active nonlinear vibration mounting systems based on vibratory power tranmission,'' J. Sound Vib. **194**, 295–316 (1996).
[9] T. D. Gillespie, *Fundamentals of Vehicle Dynamics* (Society of Automotive Engineers, Warrendale, PA, 1992).
[10] T. C. Lim, ''Case history: Finite element and experimental modeling approaches for automotive noise control problems,'' Noise Control Eng. J. **44**, 245–248 (1996).
[11] D. A. Swanson, L. R. Miller, and M. A. Norris, ''Multidimensional mount effectiveness for vibration isolation,'' J. Aircraft **31**, 188–96 (1994).
[12] G. Kim and R. Singh, ''Nonlinear analysis of automotive hydraulic engine mount,'' Trans. ASME, J. Dyn. Syst. Meas. **115**, 482–487 (1993).
[13] G. Kim and R. Singh, ''A study of passive and adaptive hydraulic engine mount systems with emphasis on nonlinear characteristics,'' J. Sound Vib. **179**, 427–53 (1995).
[14] J. E. Colgate, C.-T. Chang, Y.-C. Chiou, W. K. Liu, and L. M. Keer, ''Modeling of a hydraulic engine mount focusing on response to sinusoidal and composite excitations,'' J. Sound Vib. **184**, 503–28 (1995).
[15] T. J. Royston and R. Singh, ''Periodic response of mechanical systems with local nonlinearities using an enhanced Galerkin technique,'' J. Sound Vib. **194**, 243–263 (1996).
[16] M. Urabe and A. Reiter, ''Numerical computation of nonlinear forced oscillations by Galerkins's procedure,'' J. Math. Anal. Appl. **14**, 107–140 (1966).
[17] T. J. Royston and R. Singh, ''Experimental study of mechanical systems with mean-loaded localized continuous stiffness nonlinearities,'' J. Sound Vib. **198**, 279–298 (1996).